Arabian Journal for Science and Engineering (2019) 44:4119–4129
https://doi.org/10.1007/s13369-018-3335-7

RESEARCH ARTICLE - CIVIL ENGINEERING

Study on the Failure Characteristics of Concrete Specimen Under Confining Pressure

Chaojie Wang[1,2] · Shengqiang Yang[1,2] · Xiaowei Li[1,2] · Chenglin Jiang[1,2] · Mengkun Li[1,2]

Received: 28 April 2017 / Accepted: 22 May 2018 / Published online: 4 June 2018

Abstract
The fracture patterns of brittle materials in different stress loading modes are different. In order to study the fracture characteristics of brittle materials under confining pressure, in this study, both uniaxial compression tests and loading confining pressure tests were conducted on three concrete samples of different strengths, respectively. Meanwhile, the failure process of the samples during the loading of confining pressure was monitored using an acoustic wave tester; finally, the failure characteristics of the concrete samples were further investigated on a mesoscopic level by carrying out numerical simulations. The test results show that different failure modes were revealed in the concrete samples subjected to uniaxial compression: The failure initially started at both ends and then gradually extended to the middle part along the longitudinal direction; eventually, splitting failure, single inclined plane shear failure and conjugated inclined plane shear failure occurred. However, as the confining pressure was loaded, the samples failed merely in a simple mode, that is, the fractures occurred around the middle parts of the samples, perpendicular to the specimens axis. According to the acoustic measurements, the local failure processes before fracturing under confining pressure were consistent with those under uniaxial compression. The simulation results suggest that the failure initially started inside the samples due to the effects of longitudinal tensile stress under confining pressure, and then, it gradually extended to both sides along the lateral direction.

Keywords Tensile stress · Damage · Dynamic disaster · FLAC · Ultrasonic wave

1 Introduction

Prior to being mined, most of both the underground coal and rock masses are stable under a three-dimensional compression stress state. However, affected by excavation and mining, this state of stress equilibrium is disturbed, after which a new equilibrium state is developed under the new stress distribution subsequently. As the stress re-equilibrates, the coal and rock may fail due to the effect of yield stress, generally resulting in a variety of failure behavior, including roof falling and rib spalling. In addition, dynamic disasters such as rock bursts and coal and gas outbursts may also occur [1–6]. Therefore, studying the failure characteristics of coal and rock under different stress conditions is conducive to the maintenance of underground roadways and the interpretation of the mechanisms for dynamic disasters such as rock bursts and coal and gas outbursts.

To date, various research groups have carried out numerous experimental research on the failure characteristics of coal and rock under uniaxial, biaxial and triaxial compression, as well as direct tension. When coal and rock are subjected to these compression and tension, failure may occur in a variety of forms, including splitting failure, single inclined plane shear failure, conjugated inclined plane shear failure and tension failure [7,8]. Coal and rock masses are heterogeneous bodies comprised of pores and a variety of mineral components. As such, they have complex structures and possess characteristics such as anisotropy and discontinuity [9,10]. Since concrete is similar to coal and rock in terms of internal structure, the concrete samples showed the same failure modes as the coal and rock when the uniaxial and triaxial compression tests were performed [11–13].

✉ Chaojie Wang
superj_wang@163.com

✉ Shengqiang Yang
453526930@qq.com

1 Key Laboratory of Gas and Fire Control for Coal Mines, Ministry of Education, China University of Mining and Technology, Xuzhou, 221116 Jiangsu, China

2 School of Safety Engineering, China University of Mining and Technology, Xuzhou, 221116 Jiangsu, China

Many theoretical researches have been carried out to further investigate the failure processes of concrete and coal and rock subjected to different stress conditions. Cusatis et al. [14] and Caballero et al. [15] established a mechanical model based on a three-dimensional lattice which was proved to be highly suitable for describing the failure processes in concrete samples under uniaxial, biaxial and triaxial compression, as well as tension. Cicekli et al. [16] constructed a plastic-damage constitutive model to analyze the failure behavior under tension and compression. Yu et al. [17] studied the acoustic emission from rocks in a state of failure due to the effect of direct tension, splitting and uniaxial compression. Yang et al. [18] established a creep failure model for coal masses under triaxial compression. Using a discrete element method, Jiang et al. [19] proposed a bonding model between particles and simulated the characteristics of crack propagation in samples under uniaxial and biaxial compression, direct tension and the conditions used in Brazilian splitting tests. Zhou et al. [20] studied the influence of microfractures on the velocity of ultrasonic waves that passed through coal and rock before the failure of coal and rock under confining pressure loading. Xu et al. [21] carried out experiments on coal failure under shear loads and analyzed the evolution of the failure process on macroscopic and mesoscopic scales. Rodríguez et al. [22] investigated the failure characteristics of marble and granite under radial compression using an acoustic emission technique.

However, when coal and rock roadways are mined underground, the coal and rock surrounding the tunneling faces become exposed. The coal and rock adjacent to the exposed faces are generally subjected to bidirectional compression which is similar in magnitude to mere confining pressure [2]. However, the failure characteristics of coal and rock under this stress state (i.e., only under confining pressure) are rarely studied. Investigating the fracturing of coal and rock under confining pressure is helpful to excavation and the improvement of stability of coal and rock roadways. Moreover, it provides certain guiding principles that are useful for studying the mechanisms for dynamic disasters (such as coal and gas outbursts), which can help prevent such disasters from occurring. In this study, failure tests were conducted first on concrete samples under uniaxial compression. Then, the characteristics of the damage and fracturing occurring in concrete samples under different confining pressures were studied by using a homemade device and combining confining pressure variation with acoustic measurements. Finally, numerical simulations were performed using FLAC^{3D} software, the results of which were compared with the experimental results. In this way, the macrofracture behavior of the samples under a confining pressure was analyzed on a mesoscopic level.

2 Experiments

2.1 Preparation of Concrete Samples

The concrete samples were prepared by mixing Portland cement with fine sand. The chemical composition of Portland cement is shown in Table 1. The components of the fine sand are mainly composed of quartz and feldspar, and their content ratios are 47.7, 33%, respectively. In addition, there are also a small amount of calcite and mica included in the sand. The particle size distribution of fine sand is shown in Table 2. Three cement-to-sand ratios were adopted: 1:1 (labeled 'A'), 1:3.5 (labeled 'B') and 1:6 (labeled 'C'). According to the standards for testing mechanical parameters determined by the International Society for Rock Mechanics [23] and other previous researches [7,12], the concrete samples were divided into two groups with different sizes, namely the samples measured 50 mm × 100 mm (diameter × height) and the ones measured 110 mm × 150 mm. There were three samples in each group. The smaller samples were used for the failure tests under uniaxial compression, and the larger ones were used in the confining pressure tests. In order to accurately meet the chosen requirements, cubic concrete blocks were first prepared, and then cores drilled from these blocks were polished to produce the final samples (see Fig. 1).

2.2 Uniaxial Compression Tests

The uniaxial compression tests were conducted on the concrete samples using a commercially available rock mechanics testing system (MTS Model 815, USA). Axial loads were applied using the axial displacement control, and the loading rate was 0.5 mm/min.

2.3 Confining Pressure Experiments

Figure 2 illustrates the device created to perform the confining pressure loading tests. The device consists of a pressure cylinder, a pressure gauge, a manual hydraulic pump and an acoustic wave tester. A sample sealed by the rubber cylinder was fixed in a sealed cabin. Then, both ends of the sample were subjected to tiny axial pressure to keep the ultrasonic probe and the sample in close contact. The sample was subjected to circumferential pressure from the hydraulic oil between the rubber cylinder and the sealed cabin. As acoustic waves pass through microfractures, they are reflected, refracted, scattered and vibrated. As a result, the energy of the acoustic waves is attenuated. Moreover, the velocity of the waves gradually falls as the fracturing degree increases.

Up to the present, the use of ultrasound to detect coal and rock failure has produced very good results [20,22]. In our experiments, the acoustic wave tester was used in a mode

Table 1 Chemical composition of Portland cement

Composition	SiO_2	Al_2O_3	CaO	MgO	SO_3	Fe_2O_3	Loss of ignition
Content ratio (%)	22.7	5.02	63.12	1.45	2.24	4.37	1.19

Table 2 The particle size distribution of sand

Sieve pore diameter (mm)	4.75	2.36	1.18	0.6	0.3	0.15
Residue on sieve (%)	5	17.8	32.5	51.3	73.7	93.5

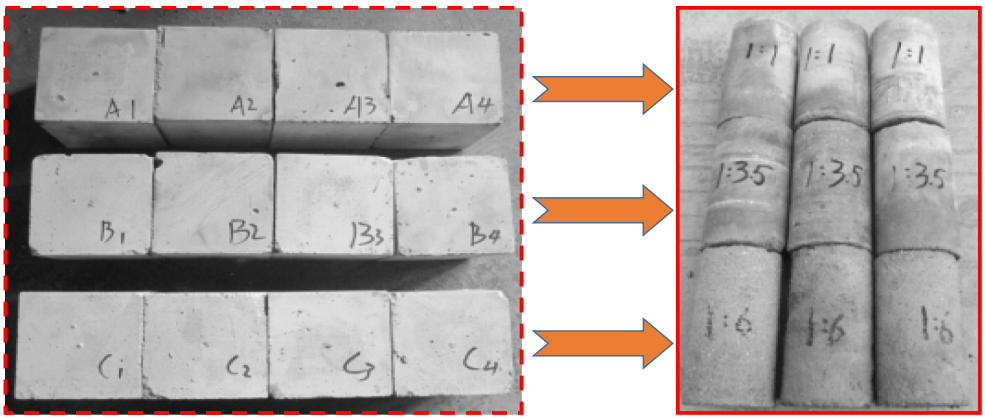

Fig. 1 The prepared concrete samples

involving continuous acoustic triggering and single measurements. The pulses transmitted corresponded to a voltage of 160 V and a width of 0.2 μs. The pressure-bearing transducer used for ultrasonic testing was equipped with a probe that was 40 mm in diameter. The sample to be tested was placed inside the pressure cylinder, and Vaseline was uniformly smeared onto its two ends. Then, longitudinal wave transducers were attached to both ends of the sample. Pressure was applied with the hydraulic pump, and the pressure values were determined through the pressure gauge. Measurements were taken at each pressure rise of 0.5 MPa until the sample fractured. Acoustic signals were sent by the transmitter, and the data were recorded after stabilization of signals. The position where the longitudinal waves passed through the interior of the sample at the fastest speed was found, and the P-wave velocity was calculated according to data recorded at that position. After measuring a set of samples, the pressure was relieved, and new samples were tested. Then, the above steps were repeated for the new specimens.

3 Experimental Results and Analysis

3.1 Uniaxial Compression Test Results

Figure 3 displays the complete set of stress–strain curves obtained in the uniaxial compression tests. The mechanical parameters of the samples subsequently derived from the stress–strain curves are shown in Table 3.

As shown in Fig. 3, in the early stage of loading, the stress in the concrete samples changed only slightly, while the strain changed greatly. With the further increase in stress, the strain increased approximately linearly as well. Then, the stress changed slightly again, while the strain changed significantly. Overall, the lower the compressive strength of the concrete samples, the more obvious the trends described above. Eventually, the stress reached a peak value, after which the stress decreased sharply with strain. The variation observed in the stress–strain curves corresponds to the following stages: compaction (microfractures and large pores in the sample become closed up), elastic deformation (the skeleton of the sample deforms elastically), yield (the original internal pores extend and new cracks develop) and failure (cracks penetrate and tear the sample apart) [8]. As can be seen from Table 3, concrete samples with the same cement-to-sand ratio had different compressive strengths, elastic moduli and Poisson's ratios, and the results were discrete. As the sand content increased (A→B→C), the compressive strength and elastic modulus of the concrete decreased significantly. At the same time, the Poisson's ratio only changed slightly (generally in the range 0.17-0.2). A rise in sand content led to the reduced strength of a concrete sample. In addition, the stress declined gradually after reaching its peak, showing an obvious strain softening property.

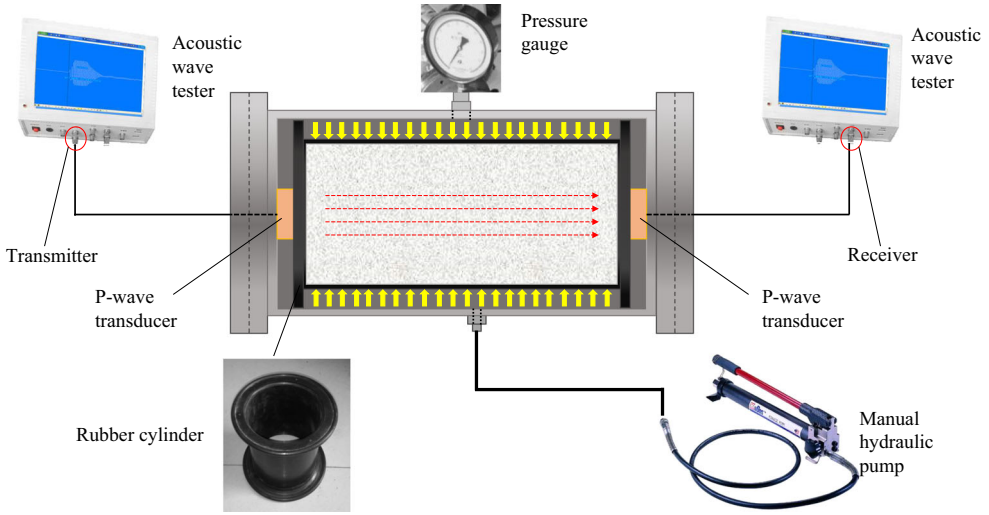

Fig. 2 Schematic diagram of the device used in the confining pressure tests

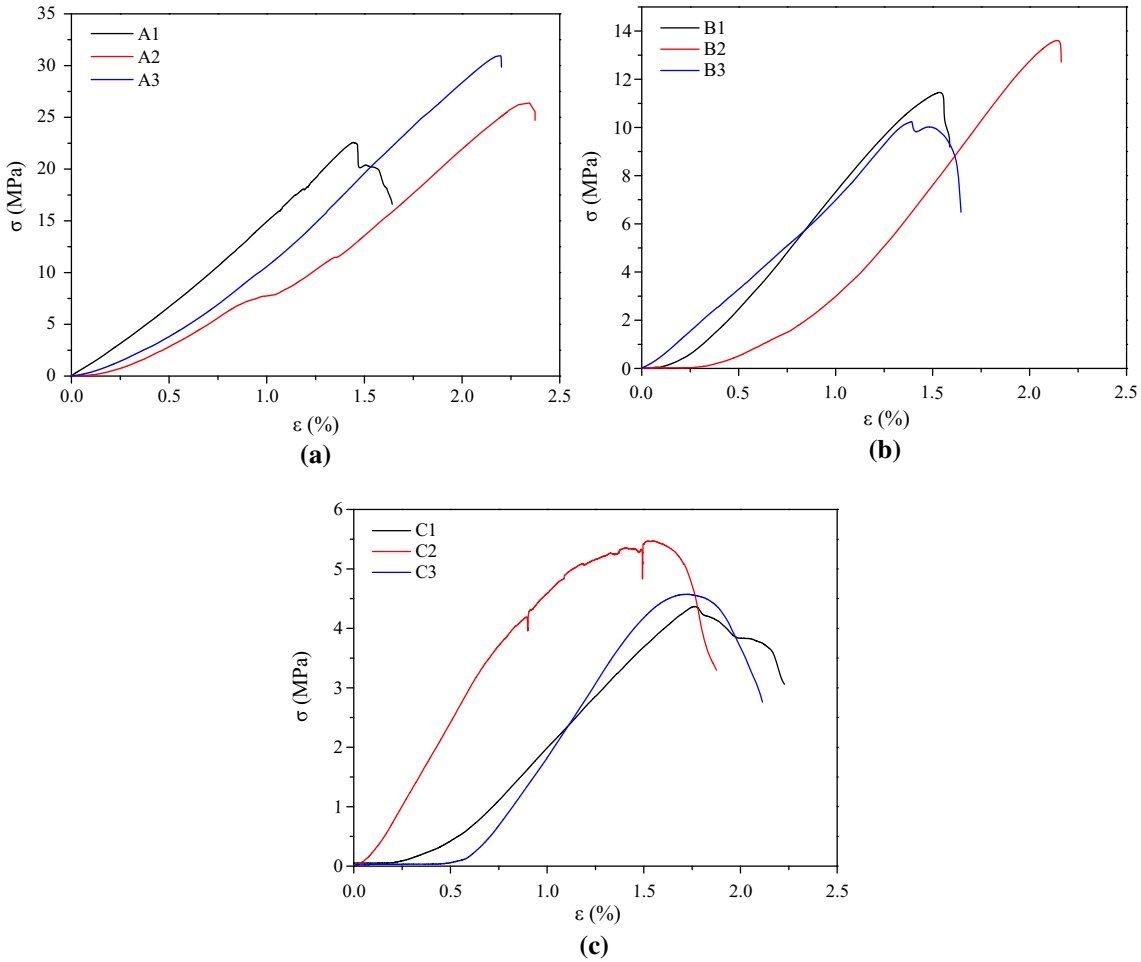

Fig. 3 The stress–strain curves obtained from three concrete samples of different strengths in the uniaxial compression tests. **a** Concrete sample A(1:1), **b** Concrete sample B(1:3.5) and **c** Concrete sample C(1:6)

Table 3 Mechanical parameters of the nine concrete samples of type A, B and C (with cement-to-sand ratios of 1:1, 1:3.5 and 1:6, respectively)

Group	Sample	Compressive strength, σ_c (MPa)		Elastic modulus, E (GPa)	Poisson ratio (μ)	
6pt		Sample	Average		Sample	Average
A	A1	22.58	25.95	1.76	0.163	0.193
	A2	25.46		1.67	0.219	
	A3	29.83		1.66	0.198	
B	B1	11.36	11.7	0.98	0.175	0.178
	B2	13.50		1.05	0.186	
	B3	10.23		0.74	0.174	
C	C1	4.32	4.75	0.34	0.184	0.198
	C2	5.39		0.53	0.196	
	C3	4.55		0.49	0.215	

Photographs and sketches of the cracks that appeared in the concrete samples after failure are shown in Fig. 4. The photographs (Fig. 4a) suggest that even though the concrete samples had different compressive strengths, they all showed almost the same failure modes under uniaxial compression, including splitting failure, single inclined plane shear failure and conjugated inclined plane shear failure. Moreover, the failure modes of samples with the same composition ratio were not always the same, and discrete fracture faces were formed. The sketch maps (Fig. 4b) show that the cracks produced after the failure consisted of macrocracks that were parallel to the loading direction or inclined at a certain angle to the loading direction. The rupture angles were generally larger than 45°. Besides, no obvious fracture was inspected in the crack sketched of samples, indicating that the new cracks were produced at both ends and in the middle parts during the damaging process. Generally, the cracks were generated at the ends before extending to the middle parts of the samples.

3.2 Confining Pressure Results

Unfortunately, when the confining pressure applied to sample A(1:1) reached 11 MPa, the rubber cylinder inside the pressure loading apparatus became fractured, and hydraulic oil leaked out. The samples were not cracked. Under such conditions, the loading process was forced to stop. For samples B(1:3.5) and C(1:6), however, clear sounds were heard, and the samples had been cracked when the confining pressure reached 4 and 3 MPa, respectively. Thus, these experiments could be ended at these stages. The failure modes observed in the B/C concrete samples after loading are shown in Fig. 5. Fracture faces parallel to the loading direction were formed in the concrete samples due to the loading of confining pressure. From the forms of the fractures, their failures were similar to tension fracture, and macrocracks could hardly be found on the concrete samples surfaces. The fracture in sample B(1:3.5) was approximately located in the middle of the sample (1/2 of the height), while that in sample C(1:6) was at around 1/3 of the height (toward the upper end).

Figure 6 shows how the average velocity of P-wave varied in the concrete samples with different strengths during the loading process. As shown in Fig. 6, at each confining pressure, the velocity of P-wave was higher in concrete samples of higher compressive strength. The initial average velocities in samples A–C were 3574, 2567 and 2436 m/s, respectively. For samples B and C (which fractured), the changes in velocity reflected the whole loading process. Thus, their graphs could be divided into three stages (I–III) from initial loading to fracturing of the sample (see the inset in Fig. 6). In Stage I, the velocity of P-wave increased linearly with the increase in loading stress (the rising trend slowed down toward the end). In Stage II, the velocity decreased as the stress increased further due to the confining pressure. Further loading eventually led to a sharp fall in the velocity of P-wave, which was Stage III. The results of sample A can also be divided into three stages. Stage I—the velocity increased approximately linearly with loading stress (low confining pressure). Stage II—the velocity changed slightly and was basically stable as confining pressure increased. Stage III—the velocity dropped gradually as confining pressure increased.

4 Numerical Simulation of Concrete Samples Subjected to a Confining Pressure

For the simulation of the yield characteristics of materials, the mixed discrete element method adopted by the FLAC^{3D} software package is much more reasonable than the finite element method. Using FLAC^{3D} (v5.0) software, this study simulated the stress states and damage characteristics of samples of ratios B and C under different confining pressures. The size of the model constructed is 110 × 150 mm (diame-

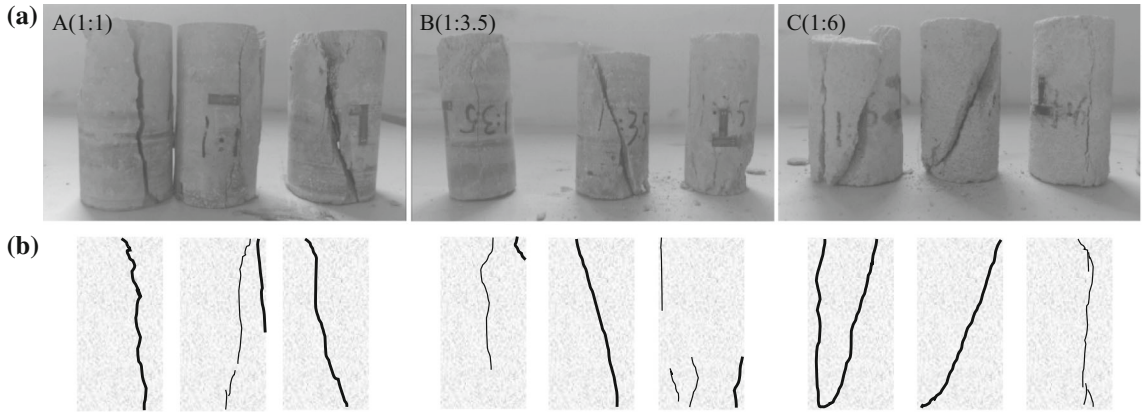

Fig. 4 Failure modes and sketches of the cracks of concrete samples in the uniaxial compression tests

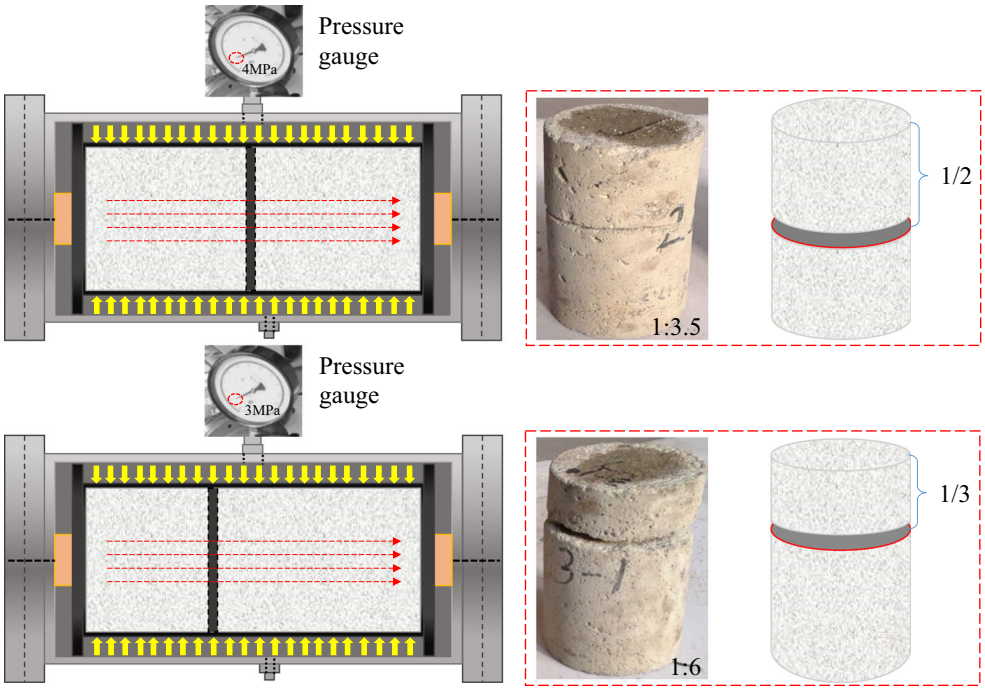

Fig. 5 The fracture modes in the concrete samples caused during the loading of confining pressure

ter × height). In order to eliminate the end effects from both ends of the samples, the confining pressure was applied in a trapezoidal form. As the simulated objects were axisymmetric, only a quarter of each cylinder was needed to observe the damage characteristics. Distributed asymptotically, the meshes were refined on the edges (a cylinder was divided into 22,500 meshes in total). The mesh division of the simulated sample is shown in Fig. 7.

The tensile strength of brittle materials such as rock is far smaller than their compressive strength (the latter is generally 8–12 times that of the former) [17]. Since the damage criteria for brittle materials accord with the Mohr stress criteria, the cohesive force and tensile strength values used in the simulations were calculated according to the compressive strength of concrete samples given in Table 3. In order to make our simulations as close to the experimental results as possible, each sample was modeled three times in accordance with their tensile–compressive strength relationship. The specific parameters are collated in Table 4.

4.1 Tensile Stress Distribution

In the simulations, the confining pressure was loaded onto the models of samples B and C at 0.1 MPa per step, and 10 groups of results were obtained from each simulation. The results show that the simulation results are the most consistent with the experimental results when the compressive strength is 10 times that of the tensile strength. When confining pressure is

Table 4 Some of the parameters used in the simulations

Stress ratio (σ_t/σ_c[a])	Sample B model		Sample C model	
	Cohesive force (MPa)	Tensile strength (MPa)	Cohesive force (MPa)	Tensile strength (MPa)
8	6.84	1.46	3.08	0.596
10	4.75	1.17	2.05	0.475
12	3.05	0.98	1.24	0.396

[a] σ_c and σ_t represent the compressive strength and tensile strength of the rock pillars, respectively

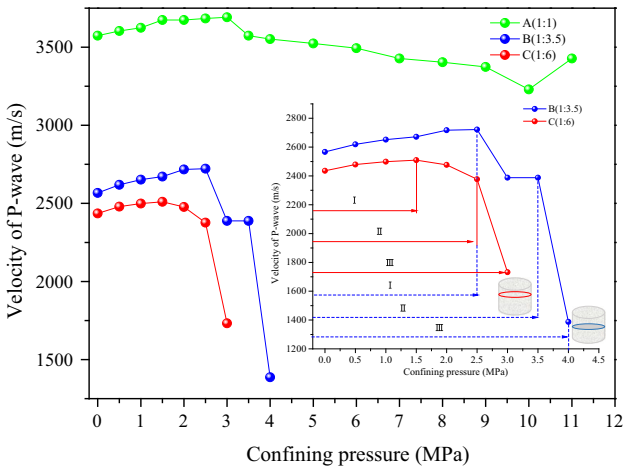

Fig. 6 Change in velocity of the P-wave in the concrete samples highlighting the failure process

applied to a sample, the tensile stress in the sample should be parallel to the sample's axis. Therefore, three typical groups of numerical simulation results were selected to compare the change of axial stress in the center of the cylinder with the confining pressure (Fig. 8).

As can be seen from Fig. 8, the maximum axial stress increases with the confining pressure. When the confining pressure reaches 2.7 MPa, the maximum axial stress in the center of the sample reaches the tensile strength (1.17 MPa) of sample B. Similarly, when the confining pressure is 1.9 MPa, the maximum axial stress in the center of the sample C reaches the tensile strength (0.475 MPa) of sample C. In addition, when the tensile stress in the sample is equal to the tensile strength under the confining pressure, further increase in the confining pressure causes the area under the axial stress curve to increase, but the maximum axial stress remains unchanged.

4.2 Damage Characteristics

Figure 9 displays the simulated cross sections of two samples of different strengths highlighting the changes occurring in the damaged area caused by the confining pressure. It can be seen from Fig. 9 that when the confining pressure reaches 2.7 and 1.9 MPa (samples B and C, respectively), the samples become damaged at their centers due to the effect of tensile stress. As the confining pressure increases, the damaged areas increase in size. From the cross section (b), the new areas suffering tensile damage mainly develop along the same direction as the loading direction of confining pressure. It can also be observed that that an area of shear failure appears in sample C when the confining pressure reaches 3 MPa.

5 Discussion

5.1 Failure Characteristics of the Samples under Uniaxial Compression and Confining Pressure

Previous results demonstrate that the concrete undergoes compaction, elastic deformation, yield and failure under uniaxial compression, which also are referred to as the linear elastic, expansion, emergence of macrocracks and friction stages of cracking zones [11]. According to Fig. 3, the stress–strain curves and the physical and mechanical parameters show discreteness because of the presence and non-uniform distribution of micropores and fractures in the concrete samples. Moreover, the observed crack propagation and penetration paths were significantly different in the failure process, thus forming discrete fracture faces. As fracturing finally occurred, there were many different crack types including splitting failure, single inclined plane shear failure and conjugated inclined plane shear failure. The experiments by Sfer et al. [12] showed that concrete samples mainly undergo splitting failure during uniaxial compression and shear failure during triaxial compression. By utilizing a discrete element method, Camborde et al. [11] simulated the failure behavior of concrete under uniaxial compression, the results of which indicated that the concrete should mainly suffer conjugated inclined plane shear failure. This is because radial stress appears in the ends of the sample due to internal friction, which causes the ends to be subjected to tridirectional stress. Thus, shear stress appears at the ends of the sample and shear failure occurs. According to the crack sketches in Fig. 4, when damage occurred in the concrete samples, new cracks were formed at the ends and extended to the center of the sample. However, as shown in Fig. 5,

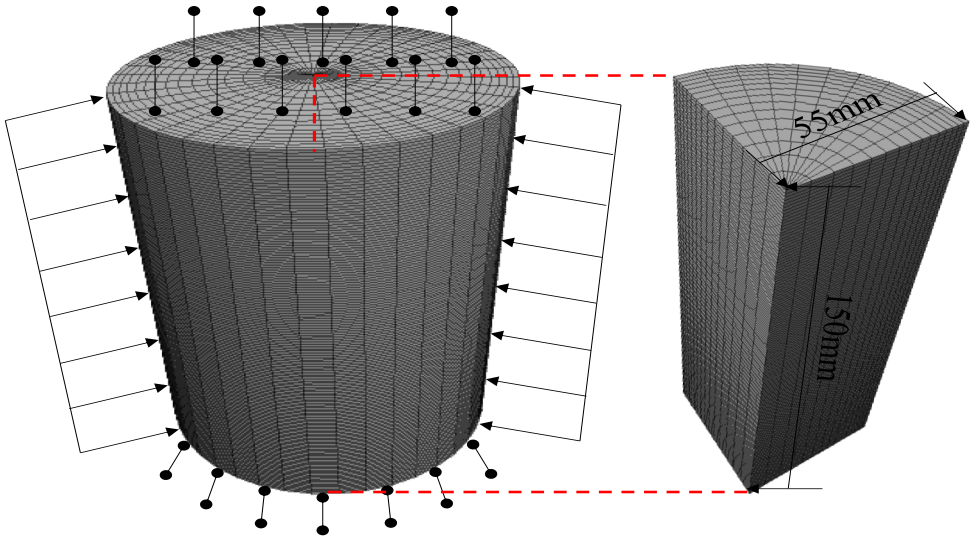

Fig. 7 Mesh generation and stress distribution in the sample model

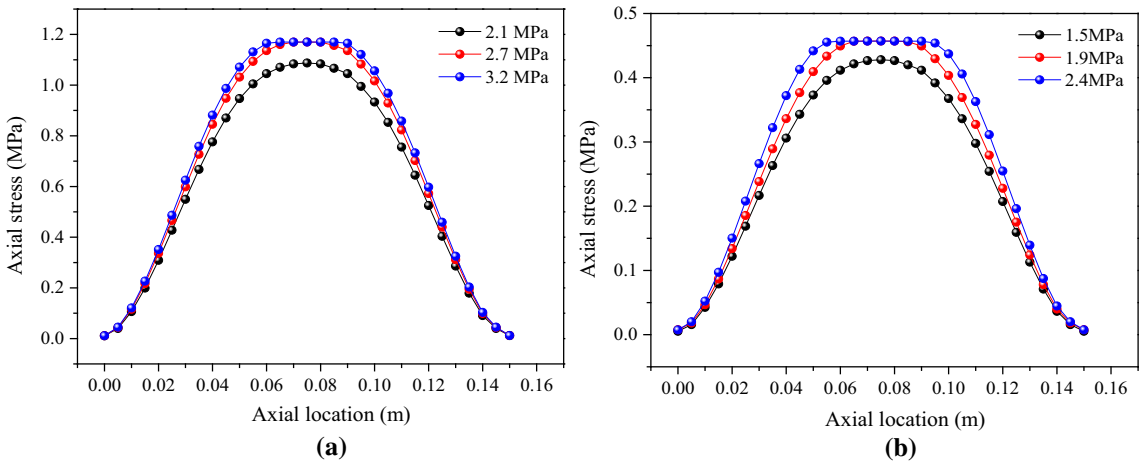

Fig. 8 The distribution of axial stress in samples subjected to various confining pressures. **a** Axial stress distribution of the rock pillars B(1:3.5) and **b** Axial stress distribution of the rock pillars C(1:6)

when a confining pressure was applied to the concrete samples, fractures occurred at locations 1/2 and 1/3 along the lengths of the samples. At the same time, no residual macrocracks were found on the outer surfaces of the samples.

5.2 Instability Failure under Confining Pressure

Acoustic waves propagate at different velocities in different media. When passing through microfractures, acoustic waves are likely to be reflected, refracted, scattered and vibrated, resulting in the energy loss of acoustic waves. Waves also move slower when they pass through rocks containing greater numbers of fractures [24]. The more compacted the rock structure is, the faster the acoustic waves pass through the rock. According to Fig. 6, there are three distinct stages that can be found in the P-wave velocity vs. confining pressure graphs. In Stage I, fractures and micropores in the concrete samples are compacted and closed up under the low confining pressure applied. This increases the compactness of the concrete samples, and thus, the velocity of P-wave gradually increases. As the confining pressure is further increased to a certain extent, a point is reached where the fractures and pores in the samples have almost reached their maximum degree of closure (corresponding to the largest deformation strength). In other words, nearly all the fractures and micropores vertical to the loading direction are closed, and meanwhile, those parallel to the loading direction have reached their maximum elastic deformation capacity at this time. At this point, the P-wave velocity has its largest value. In Stage II, when the confining pressure reaches around 2.5 and 1.5 MPa (for samples B and C, respectively), the tensile stress produced under the confining pressure extends the microfractures that are par-

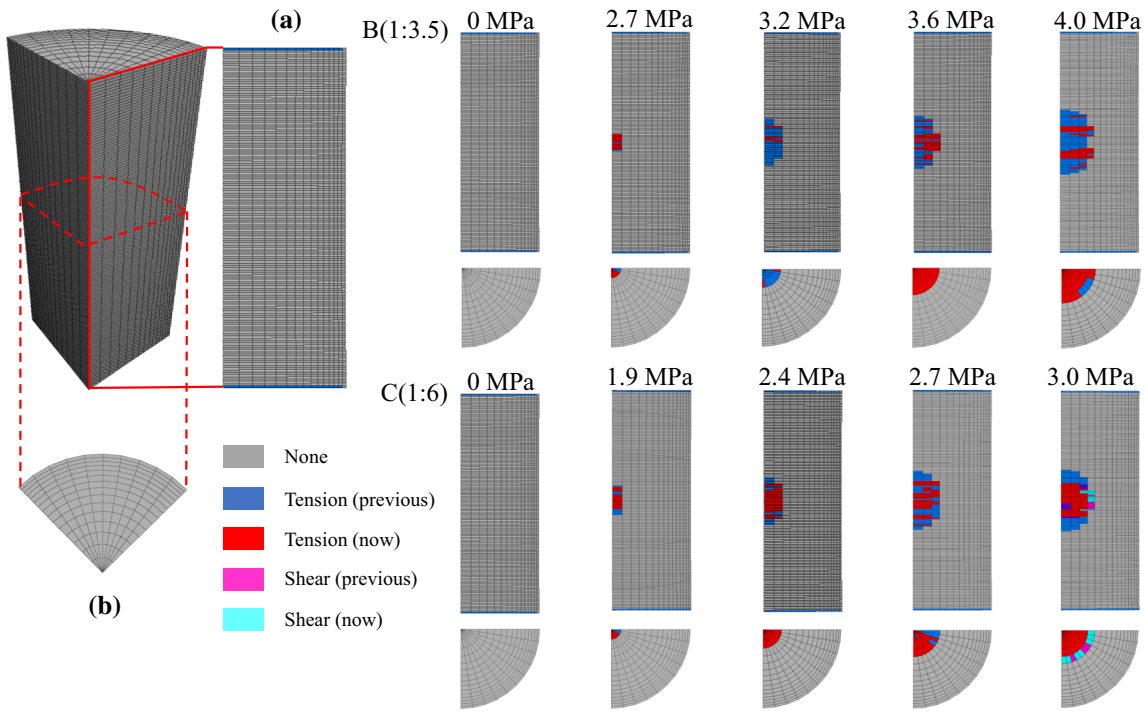

Fig. 9 The evolution of the damage in the samples as the confining pressure increases

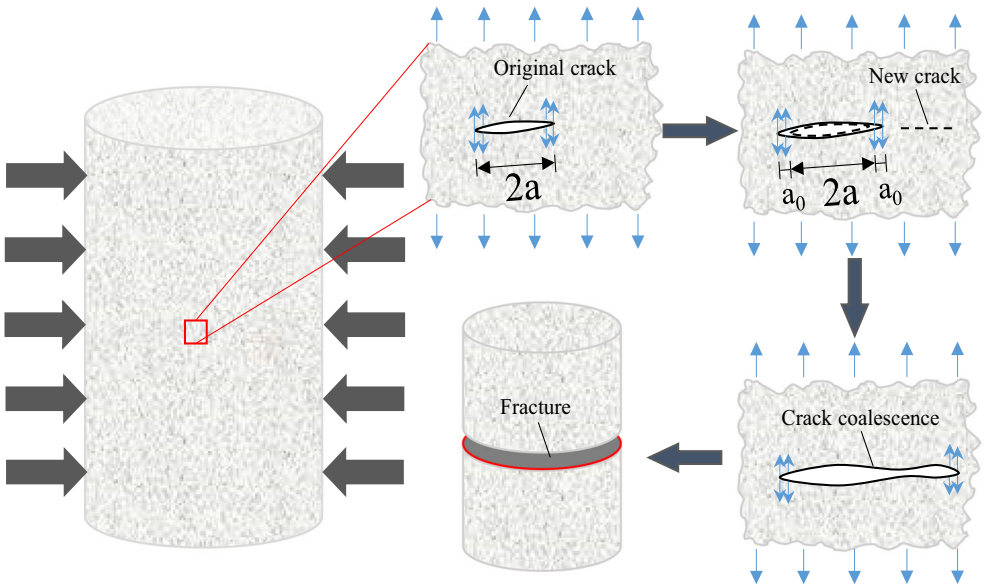

Fig. 10 Sketches illustrating the fracturing of a concrete sample under confining pressure

allel to the loading direction of the confining pressure. With further loading, new cracks are generated and connected to the original ones (so the *P*-wave velocity drops). In Stage III, as the confining pressure increases further still, the new and original cracks become connected to form macrofractures which cause the sample to tear and fracture, thus forming fracture faces that are approximately parallel to the loading direction of the confining pressure. Therefore, in the confining pressure experiments, the damage and failure processes occurring are roughly consistent with the behavior under uniaxial compression (compaction, elastic deformation, yield and failure).

The numerical simulations suggest that when the compressive strength is 10 times that of the tensile strength (see Fig. 9), localized damage occurs in the center of the sample under the confining pressures of 2.7 and 1.9 MPa (for

concrete samples B and C, respectively). This coincides well with the P-wave velocity changes when the experimental pressures were 2.5 and 1.5 MPa (which we suggest are due to local damage appearing in concrete samples B and C). The main difference between the simulated and experimental results is that tensile fracture had occurred experimentally when the confining pressure reached 4 and 3 MPa, whereas the samples were fractured continuously but incompletely along the horizontal direction at these pressures according to the simulations. This is because the simulation software is able to simulate the damage processes in brittle materials, but it is unable to describe instantaneous tensile fracture using the constitutive stress–strain equations of the brittle materials.

Figure 9 shows that the samples become damaged at their centers due to the effects of tensile stress at sufficiently high confining pressures (2.7 and 1.9 MPa in the samples shown). As the confining pressure increases further, the damaged areas increase in size. New tensile failure areas are developed mainly along the direction of loading (see the cross sections in Fig. 9), thus generating fractures parallel to the loading direction. When the tensile stress in the sample (due to the confining pressure) reaches the sample's tensile strength (Fig. 8), the maximum axial stress in the sample becomes fixed, while the initially damaged area becomes larger gradually as the confining pressure increases. This means that once the tensile stress on the concrete is larger than the tensile strength, new cracks will be produced which quickly become extended and interconnected with the original ones. This also explains why instantaneous fractures generally occur in brittle materials under tensile stress. This is different to what happens under compressive stress where concrete samples are fractured after the extension and enrichment of cracks along a certain direction.

According to the simulation results shown in Fig. 9, under confining pressure, the concrete suffers tensile failure generally under tensile stress. Under tensile stress, the stress is concentrated at the ends of the cracks regardless of the angle between the long axis of crack and stress direction (except when the long axis is parallel to the stress). As long as the tensile stress satisfies Eq. (1), the crack will extend along the direction perpendicular to the stress, which will rapidly result in the occurrence of concrete sample fracturing failure [25].

$$\sigma = \frac{K_{\mathrm{I}}}{\sqrt{2\pi r}} \tag{1}$$

where σ is the tensile stress at the end of the crack; K_{I} is the stress intensity factor of concrete; and r is the distance of any point surrounding cracks from the end of cracks. A sketch illustrating the fracture process of concrete samples during loading confining pressure is shown in Fig. 10 where the fractal nature of the crack has been ignored and its surfaces have been assumed to be smooth [26].

6 Conclusions

The main failure modes of concrete (brittle materials) subjected to compressive stress are splitting and shear failure. In order to understand the failure characteristics of brittle materials under confining pressure, the failure tests were conducted on three concrete samples of different strengths under confining pressure and uniaxial compression, respectively, in this paper. Additionally, in order to monitor the samples during the loading of a confining pressure, a device incorporating an acoustic wave tester was developed. The following conclusions can be drawn:

(1) Under uniaxial compression, cracks were initiated at the top, in the middle or at the bottom of the samples and the main cracks became extended along the loading direction until they were connected. The main failure modes included splitting failure, single inclined plane shear failure and conjugated inclined plane shear failure. During the loading of a confining pressure, however, fractures only occurred near the middle parts of the samples. The data obtained via P-wave monitoring provide evidence that the process of fracturing failure in the samples consists of several steps: compaction, elastic deformation, yield and final failure.
(2) The numerical simulations show that when the compressive strength of a sample is 10 times that of its tensile strength, the confining pressure values required for the occurrence of localized damage are in good agreement with the experimental values. In addition, the concrete is subjected to tensile stress perpendicular to the loading direction under the confining pressure. Furthermore, affected by the tensile stress, cracks first appear in the middle part, then extend along the loading direction and become connected, and finally tensile fracturing failure occurs in the sample.

Acknowledgements The authors are grateful to the financial support from the Fundamental Research Funds for the Central Universities (2017CXNL02) and the Priority Academic Program Development of Jiangsu Higher Education Institutions (PAPD). The authors would like to thank the editors and the anonymous reviewers for their careful review of this paper.

References

1. Bai, Q.S.; Tu, S.H.; Chen, M.; Zhang, C.: Numerical modeling of coal wall spall in a longwall face. Int. J. Rock Mech. Min. Sci. **88**, 242–253 (2015)

2. Jiang, C.L.; Yu, Q.X.: The Spherical Shell Instability Mechanism and Prevention Technology of Coal and Gas Outburst. China University of Mining and Technology Press, Xuzhou (1998)
3. Wang, C.J.; Yang, S.Q.; Jiang, C.L.; Yang, D.D.; Zhang, C.J.; Li, X.W.; Chen, Y.J.; Tang, J.: A method of rapid determination of gas pressure in a coal seam based on the advantages of gas spherical flow field. J. Nat. Gas Sci. Eng. **45**, 502–510 (2017)
4. Lawson, H.E.; Tesarik, D.; Larson, M.K.; Abraham, H.: Effects of overburden characteristics on dynamic failure in underground coal mining. Int. J. Min. Sci. Technol. **27**, 121–129 (2017)
5. Zhou, A.T.; Wang, K.; Fan, L.P.; Kiryaeva, T.A.: Gas-solid coupling laws for deep high-gas coal seams. Int. J. Min. Sci. Technol. **27**, 675–679 (2017)
6. Zuo, J.P.; Chen, Y.; Cui, F.: Investigation on mechanical properties and rock burst tendency of different coal-rock combined bodies. J. China Univ. Min. Technol. **47**(1), 81–87 (2018)
7. Medhurst, T.P.; Brown, E.T.: A study of the mechanical behaviour of coal for pillar design. Int. J. Rock Mech. Min. Sci. **8**, 1087–1105 (1998)
8. Wu, Y.P.; Gao, X.C.: Experimental comparative study on lateral deformation characteristics of coal sample in different loading path. J. China Coal Soc. **35**, 44–48 (2010)
9. Kong, X.G.; Wang, E.Y.; Hu, S.B.; Liu, X.F.; Xu, Z.Y.; Zhan, T.Q.: Research on precursory characteristics of critical slowing down before the failure of coal samples containing methane. J. China Univ. Min. Technol. **46**(1), 1–7 (2017)
10. Chen, W.X.; He, X.Q.; Liu, M.J.; Mitri, H.; Wang, Q.: Meso- and macro-behaviour of coal rock: observations and constitutive model development. Int. J. Min. Reclam. Environ. **30**(1), 13–24 (2013)
11. Camborde, F.; Mariotti, C.; Donze, F.V.: Numerical study of rock and concrete behaviour by discrete element modelling. Comput. Geotech. **27**, 225–247 (2000)
12. Sfer, D.; Carol, I.; Gettu, R.; Etse, G.: Study of the behavior of concrete under triaxial compression. J. Eng. Mech. **2**, 156–163 (2002)
13. Grassl, P.; Jirásek, M.: Meso-scale approach to modelling the fracture process zone of concrete subjected to uniaxial tension. Int. J. Solids Struct. **47**, 957–968 (2010)
14. Cusatis, G.; Bažant, Z.P.; Cedolin, L.: Confinement-shear lattice model for concrete damage in tension and compression: I. Theory. J. Eng. Mech. **12**, 1439–1448(2003)
15. Caballero, A.; Lo'pez, C.M.; Carol, I.: 3D meso-structural analysis of concrete specimens under uniaxial tension. Comput. Methods Appl. Mech. Eng. **195**, 7182–7195 (2006)
16. Cicekli, U.; Voyiadjis, G.Z.; Al-Rub, R.K.A.: A plasticity and anisotropic damage model for plain concrete. Int. J. Plast. **23**, 1874–1900 (2007)
17. Yu, X.B.; Xie, Q.; Li, X.Y.; Wang, Q.R.; Song, Z.P.: Acoustic emission of rocks under direct tension, Barazilian and uniaxial compression. Chin. J. Rock Mech. Eng. **26**, 137–142 (2007)
18. Yang, S.Q.; Xu, P.; Ranjith, P.G.: Damage model of coal under creep and triaxial compression. Int. J. Rock Mech. Min. Sci. **80**, 337–345 (2015)
19. Jiang, M.J.; Chen, H.; Crosta, G.B.: Numerical modeling of rock mechanical behavior and fracture propagation by a new bond contact model. Int. J. Rock Mech. Min. Sci. **78**, 175–189 (2015)
20. Zhou, F.; Xu, M.J.; Ma, Z.G.; Ma, Z.G.; Cai, L.; Zhu, Z.; Li, J.: An experimental study on the correlation between the elastic wave velocity and microfractures in coal rock from the Qingshui basin. J. Geophys. Eng. **9**, 691–696 (2012)
21. Xu, J.; Cheng, L.C.; Tan, H.Y.; Wang, L.; Wu, H.: Effects of original cracks on macro-meso evolution law of coal shear failure. Chin. J. Rock Mech. Eng. **32**, 33–40 (2013)
22. Rodríguez, P.; Arab, P.B.; Celestino, T.B.: Characterization of rock cracking patterns in diametral compression tests by acoustic emission and petrographic analysis. Int. J. Rock Mech. Min. Sci. **83**, 73–85 (2016)
23. Fairhurst, C.E.; Hudson, J.A.: Draft ISRM Suggested Method for the complete stress-strain curve for the intact rock in uniaxial compression. Int. J. Rock Mech. Min. Sci. **3**, 279–289 (1999)
24. Khandelwal, M.; Singh, T.N.: Correlating static properties of coal measures rocks with P-wave velocity. Int. J. Coal Geol. **79**, 55–60 (2009)
25. Wnuk, M.P.; Yavari, A.: Discrete fractal fracture mechanics. Eng. Fract. Mech. **75**, 1127–1142 (2008)
26. Wnuk, M.P.; Yavari, A.: On estimating stress intensity factors and modulus of cohesion for fractal cracks. Eng. Fract. Mech. **70**, 1659–1674 (2003)